Complete citation:

Rowin, W. A., Hou, J., & Ghaemi, S. (2018). Turbulent channel flow over riblets with superhydrophobic coating. *Experimental Thermal and Fluid Science*, *94*, 192-204. doi: 10.1016/j.expthermflusci.2018.02.001

The final publication is available at https://doi.org/10.1016/j.expthermflusci.2018.02.001

Turbulent channel flow over riblets with superhydrophobic coating

Wagih Abu Rowin, Jianfeng Hou, Sina Ghaemi*
Department of Mechanical Engineering, University of Alberta, Edmonton, T6G 2G8 Alberta, Canada

Abstract

The performance of riblet surfaces after applying a superhydrophobic coating (SHC) is evaluated by planar particle image velocimetry (PIV) measurement at riblet tip spacing of s^+ = 8.6, 17.3 and 34.6 (normalized using wall unit). The three riblet sizes correspond to an undersized (small drag reduction), an optimum (maximum drag reduction), and an oversized (drag increase) riblet, respectively. All the experiments are carried out in a turbulent water channel flow at constant Re_H = 4,360 (based on channel height H and average velocity). The superhydrophobic layer is formed by spray coating of micro/nano particles with a thickness of ~1λ (wall unit). The results show smaller mean velocity over the s^+ = 8.6 and s^+ = 17.3 riblets when coated with the superhydrophobic layer at near-wall region of $y^+ < 15$ while the mean velocity over the s^+ = 34.6 riblet with SHC is larger relative to the non-coated counterpart. The SHC increased $\langle u^2 \rangle$ over the s^+ = 8.6 and 17.3 surfaces while $\langle u^2 \rangle$ reduced over the s^+ = 34.6 surface in the near wall region of $y^+ < 40$. A smaller $\langle v^2 \rangle$ value is observed in the near-wall region ($y^+<50$) of all three riblets upon applying the SHC while the reduction is smaller for smaller riblets. The $\langle v^2 \rangle$ peak also shifts away from the wall upon coating the s^+ = 34.6 riblet. The Reynolds shear stress over s^+ = 8.6 and s^+ = 17.3 riblets is not considerably different relative to the superhydrophobic coated counterparts while a large reduction of $\langle uv \rangle$ is observed at $y^+< 30$ after coating the s^+ = 34.6 riblet. The estimation of drag reduction (DR) based on weighted integral of $\langle uv \rangle$ shows 6.0% and 10.1% reduction of drag over the s^+ = 8.6 and s^+ = 17.3 riblets after the SHC process, respectively. SHC on the oversized s^+ = 34.6 riblet improves the performance from 9.0% drag increase (DI) over the non-coated surface to 1.2% DR, equivalent to 10.2% reduction of drag upon coating the riblet. The larger improvement of oversized riblets ($s^+>30$) is associated with the effectiveness of the SHC in the larger riblet valley and consequently attenuation of ejection and sweep motions. The SHC broadens the operation range of larger riblets, which are easier to manufacture.

Keywords:

Riblet surface, superhydrophobic surface, particle image velocimetry, turbulent water channel flow

1 Introduction

High skin-friction in turbulent flows leads to large energy consumption in transport applications such as oil pipelines, marine vessels, and aircrafts. Drag reduction (DR) techniques such as polymer additives [1], microbubbles [2], superhydrophobic surfaces [3], and riblets [4, 5] have been explored to increase the performance of these systems. Among these techniques, those that do not require any energy input, such as riblet and superhydrophobic surfaces, are of particular interest.

Riblets are microgrooves aligned in the streamwise flow direction that can reduce the skin-friction component of drag by up to ~10% [4, 6]. Their performance strongly depends on their size relative to the flow scales expressed as a non-dimensional scale s^+ defined as $s^+ = s\, u_\tau / \nu$. Here, s is the cross-flow spacing between successive riblet tips, ν is the kinematic viscosity, and u_τ is the friction velocity over a smooth surface exposed to an identical flow rate [6]. Walsh [7] observed DR when $s^+ < 30$ with maximum DR in the range of s^+ = 15 to 20. Bechert *et al.* [6] investigated a variety of groove shapes and observed increase of the DR until $s^+ \sim 17$ followed by smaller DR until it turned into DI at around s^+ = 30. García-Mayoral and Jiménez [8] suggested the square-root of groove cross-section A^+_g to characterize the optimum geometry for maximum drag reduction. Their analysis showed maximum drag reduction occurs at A^+_g = 10.7 with 10% scatter in the data collected from variety of geometries.

Several investigations associated riblet DR with the shift of the streamwise vortices away from the wall and reduction in their spanwise meandering. Streamwise vortices are known to contribute to positive turbulent production through sweep and ejection motions [9]. Suzuki and Kasagi [10] conducted a detailed analysis of the turbulent flow in the riblet valley and observed impediment of energy transfer from streamwise to spanwise turbulent kinetic energy due to suppression of the streamwise vortices. This is in agreement with the reduction of ejection and sweep motions over

* E-mail address: ghaemi@ualberta.ca (S. Ghaemi)

riblets observed by Choi *et al.* [11]. Lee and Lee [12] carried out smoke visualization in a wall-normal spanwise plane inside the riblet valley and observed that most of streamwise vortices (~$30\nu/u_\tau$ in diameter [13]) stay above the riblet valley and only interact with the riblet tip. Luchini [14] associated drag reduction with the different between the virtual origin of the spanwise (y_s) and longitudinal (y_l) flows over riblets. Luchini [14] proposed that DR occurs by impedance of streamwise vortices when y_s is further away from the wall (i.e., $y_s - y_l > 0$).

A limiting factor for practical application of riblet surfaces is the increase in drag at higher Reynolds numbers when the length-scale of the turbulent wall flow becomes smaller than the riblet spacing. This drag increase (DI) regime occurs since the smaller streamwise vortices fall into the riblet valley and expose the valley to high skin-friction events when $s^+ > 30$ [12]. The near-wall 3D-PTV measurement of Suzuki and Kasagi [10] confirmed larger wall-normal velocity gradient ($d\langle U\rangle/dy$) in the riblet valley during DI regime. According to this theory, skin-friction per unit surface area is still smaller relative to that of the smooth wall [11] while larger total skin-friction is associated with the increase of effective surface area of riblets. However, DNS of García-Mayoral and Jiménez [8] did not show any lodging of the quasi-streamwise vortices inside the grooves at DI regime. They observed formation of localized streamwise vortices above the riblet grooves in the buffer layer of DI regime while the break-down of the DR regime was associated with formation of two-dimensional spanwise rollers. It is of interest to delay the break-down of the DR regime to extend the operation range of riblets over a wider range of Reynolds numbers. In addition, riblets with large spacing are easier to manufacture and maintain. The possible extension of the operation range of riblets has been recently sought by applying a superhydrophobic layer (e.g., Barbier, Jenner, and D'Urso [15] and Prince, Maynes, and Crockett [16]).

The use of a superhydrophobic surface (SHS) was inspired by the water repellent properties of lotus leaf [17] and is synthesized by a variety of techniques such as hydrophobic treatment of a textured surface or deposition of hydrophobic materials on a flat substrate [18]. The micro size cavities of a SHS maintain small air pockets that avoid contact between the liquid and the solid surface. As a result, a shear-free interface forms when liquid flows over a SHS [19]. Experiments in laminar micro-channels over SHSs have demonstrated a slip velocity up to 60% of the average velocity [20] and up to 40% DR based on pressure drop measurement [21].

Investigation of turbulent flows over SHSs has demonstrated a wide range of DR and DI outcomes. Zhao, Du, and Shi [22] and Peguero and Breuer [23] did not observe a considerable drag reduction. Daniello, Waterhouse, and Rothstein [3] observed up to 50% DR based on pressure drop measurement over micro-patterned surfaces with 120×38 mm^2 area produced by photolithography process. Park, Sun, and Kim [26] also applied a photolithographic process over a 27×27 mm^2 silicon chip and confirmed up to 75% drag reduction. A smaller DR with larger experimental uncertainty and repeatability issues has been typically observed over larger surfaces produced by deposition of micro/nano particles. Aljallis *et al.* [24] reported drag increase in the turbulent regime. Bidkar *et al.* [25] reported cases with DI and cased with up to 30% DR over a boundary layer by direct force measurement. Ling *et al.* [27] observed maximum drag reduction of 36% using SHSs with random texture. The observed drag variation over SHSs is due to several factors including variation in slip-length of the surface [26], the scale of surface protrusions relative to the scales of the wall flow [25], and the longevity of the surfaces [28]. The latter issue is caused by dissolution of the air pockets into the shear flow and also particle-plastron impact in PIV measurements [29].

Turbulent DR over a SHS has been associated with attenuation of streamwise vortices due to the slip velocity at the surface [22]. Numerical and experimental investigations have confirmed reduction of ejection/sweep motions and Reynolds stresses over the SHS in the DR regime [30, 31]. Numerical simulation of Min and Kim [24] has shown that imposing a wall boundary condition with streamwise slip results in DR and attenuates turbulence intensities while an imposed spanwise slip results in drag increase and intensification of turbulence due to stronger streamwise vortices. However, in practice, spanwise and streamwise slip simultaneously occur (omnidirectional slip) while the spanwise component is expected to have a negative contribution to DR [24].

The combination of a riblet surface coated with a superhydrophobic layer has the potential to fulfill the shortcoming of both riblet and superhydrophobic DR [15, 16]. A superhydrophobic coating can improve the performance of oversized riblets by decreasing their effective area while riblets are expected to enhance the performance of a SHS due to smaller spanwise motion in the riblet valley. In addition, the riblet valley shields the superhydrophobic plastron in a low velocity region (thicker viscous sublayer), which may reduce dissolution of the air pockets (wall-normal momentum transport) and increase their longevity. Therefore, the combination of a riblet surface with superhydrophobic coating is of interest.

Barbier, Jenner, and D'Urso [15] applied a combination of hydrophobic polymer coatings and nano-pores formed by anodization-etching over saw-tooth riblets with 10 μm, 100 μm to 1000 μm depth. They tested the surfaces using

a cone-and-plate rheometer in turbulent regime and observed up to 20% DR over the superhydrophobic 100 μm grooves relative to the flat reference surface. The coated 10μm and 1000μm grooves showed 5% and 10% DR, respectively. However, the groove size with respect to the flow scale (i.e., s^+) was not reported and it appears that no compensation was made for the virtual origin of the riblet surfaces. Prince, Maynes, and Crockett [16] manufactured riblets with 160μm spacing covered with smaller superhydrophobic micro-ribs (28μm width). The surfaces were tested by varying Re number from 5,000 to 15,000 corresponding to $s^+ = 8$ to 20. The results showed about 7% DR using the superhydrophobic riblets (with micro-rib) at the two lowest Re numbers of 5,000 and 7,000 corresponding to $s^+ = 8$ and 10, respectively. However, the baseline riblet surface (without micro-rib) did not produce any DR at $s^+ = 8$ and 10. The superhydrophobic micro-ribs (without large ribs) also resulted in about 3% DR at Re = 5,000 and 7,000 while it failed to produce any DR at higher velocities.

The current work investigates the effect of superhydrophobic coating on undersized ($s^+ = 8.6$), optimum ($s^+ = 17.3$), and oversized ($s^+ = 34.6$) riblets at $Re_\tau = 144$. A planar PIV is applied for characterization of the turbulent flow and investigation of drag reduction mechanism. This measurement technique is also chosen due to challenges in measurement of minute skin-friction over small surface samples using direct force measurement or pressure drop measurement. A spray coating technique capable of covering large surfaces is used here to produce the SHSs. Non-coated riblets and flat surfaces (with and without SHC) are also considered as baseline configurations. The turbulence statistics over the surfaces was scrutinized to evaluate the performance of the coated riblets. The skin-friction of the surfaces is also estimated using the profile of Reynolds shear stress.

2 Experiment setup

2.1 Flow facility

The experiments were carried out in a free-surface flume with test-section dimensions of 5.2 m long and 0.68 m wide. A channel flow was developed inside this flume using a glass bottom wall and a cast acrylic top wall as shown in Fig. 1. The formed channel is 3 m long (L) in the streamwise direction (x) and has a rectangular cross-section of 25 mm (H) in the wall-normal direction (y) and 540 mm (W) in the spanwise direction (z). One of the side walls of the channel has a 4 cm viewing window at the measurement location to permit access for PIV imaging. A honeycomb was placed at the entrance of the channel to break large vortices and straighten the flow. The test surfaces were installed in an insert section with 570 mm length and 320 mm width located 1.9 m (76H) downstream of the channel entrance to ensure a fully developed turbulent flow at the measurement location.

Instantaneous and fluctuating velocity in the x, y and z directions (streamwise, wall-normal, spanwise) are denoted as U, V, W and u, v, w, respectively. The velocity averaged across the cross-section (y direction) for all the experiments was $U_b = 0.175$ m/s, which corresponds to $Re_H = 4{,}360$ based on channel height H and kinematic viscosity of $\nu = 1.004\times10^{-6}$ m^2/s. The friction velocity and the wall unit for the smooth surface are estimated using the Clauser method [25] (see section 3.1). The estimated friction velocity and wall unit over the smooth wall are $u_{\tau 0} = 0.0116$ m/s and $\lambda = 86.5$ μm, respectively. Therefore, the friction Reynolds number of the smooth channel is $Re_\tau = 144$ based on the estimated friction velocity and half channel height.

The lifetime of the air pockets in the cavities/pores of the superhydrophobic surface is a function of the amount of dissolved air in the flume and can directly affect the duration of DR [29, 33, 34]. It is also speculated that the pH level of surrounding fluid in the water flume can affect the longevity and performance of the SHS surfaces. Therefore, the oxygen level, pH, and temperature of the water channel were recorded and maintained between 8.4-8.5 mg/L, 8.0-8.1, and 21-22° C during all experiments, respectively.

2.2 Smooth and riblet surfaces without coating

Four aluminum plates with dimensions of 430 mm (17.2H) long, 280 mm wide, and 6.35 mm thick were used to manufacture the test surfaces. One of the surfaces was machined to be flat while trapezoidal riblets of three different dimensions were machined on the three other surfaces using CNC milling with 10 μm tolerance. The riblet dimensions are defined in Fig. 2 and listed in Table 1. The DR predicted based on experimental results of Bechert *et al*. [6] is also shown in Table 1. Riblet surfaces were placed such that 40% of the height of the riblet (h_p) protruded in the channel flow (as shown in Fig. 2). This is implemented based on the recommendation of Bechert and Bartenwerfer [29] and Grüneberger and Hage [30] to obtain the same outer layer velocity profile as the smooth surface. As it is predicted, $s^+ = 8.6$ results in smaller DR while $s^+ = 17.3$ has larger DR and $s^+ = 34.6$ increases drag [6].

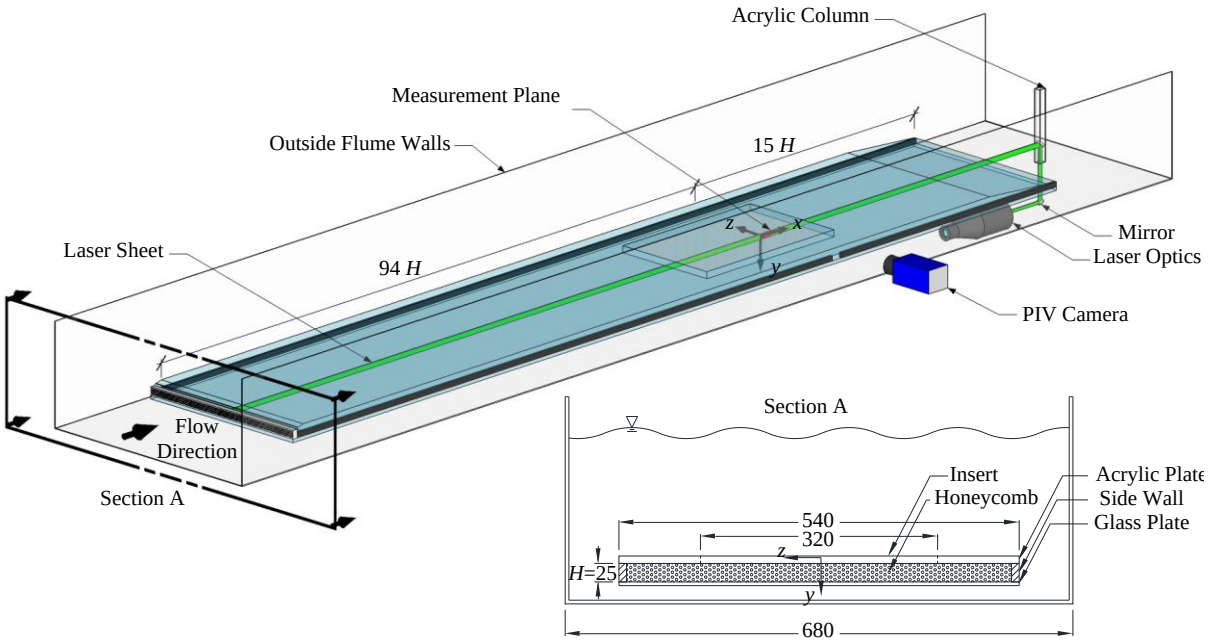

Fig. 1 A schematic of the experimental setup showing the 2D-channel submerged in the large flume, the honeycomb flow at the entrance, the insert module to place the test surface, and the PIV measurement setup. All dimensions are in mm.

Table 1 Geometric features of the riblet surfaces and DR estimated based on Bechert *et al*. [6].

s^+	s [μm]	h_t [μm]	α	DR
8.6	750	375	30˚	5%
17.3	1,500	750	30˚	8%
34.6	3,000	1,500	30˚	-6%

2.3 Riblet surfaces with superhydrophobic coating (SHC)

The superhydrophobic layer was formed by depositing a layer of micro and nano-particles on the riblet and flat surfaces using a commercial product (NeverWet, Rust Oleum). The surfaces were initially cleaned with ethanol for better adhesion of the coatings. An acrylic-based polymer solution was sprayed in four passes on the aluminum substrate as the base coat (binding layer). Each pass refers to spraying from either left to right or top to bottom of the test surface. After leaving the solvent to evaporate for about 30 min, three passes of a top-coat layer containing nano/micro particles in ethanol was applied over the base coat. The surface was left dry for 12 hours before submerging in the water channel.

Bidkar *et al*. [31] showed that DR over a SHS occurs when the surface roughness is an order of magnitude smaller than the thickness of the viscous sublayer. In the present study, the thickness of the viscous sublayer was estimated to be ~ 450 μm while the peak-to-trough roughness t_{SHC} of the surfaces was ~ 80 μm (~ one wall unit). The details of the roughness measurment can be found in Vajdi Hokmabad and Ghaemi [28]. Images of the riblet surfaces after coating are shown in Fig. 2. The thickness of the coating on the riblet walls and in the valley is relatively uniform (~0.08 mm) while accumulation of large particles is observed at the riblet tip. The presence of the air layer over the surfaces with superhydrophobic coating was verified by scrutiny of the surface immediately after the experiments. The surfaces were observed to be completely dry (non-wetted state) immediately after they were taken out of the water flume. The durability of a similar surface with SHC was investigated recently by Vajdi Hokmabad and Ghaemi [28] using the contact and roll-off angles before and after exposure to a two-phase flow of 2 μm sliver coated particles with density of 4 g/cm^3 in water at a concentration of 20-30 particles/mm^3. These particles have a relaxtion time [$\tau_p = (\rho_p - \rho_w)\, d_p^2$

/18μ] of about 0.7μs, where ρ_p, ρ_w, d_p, μ are the desnity of the particle, desnity of water, particle diameter, and water dynamic viscosity, respectively. The relaxation time of the silver coated paerticles is larger than the relaxation time (τ_p = 0.1μs) of the hollow glass tracres used in the current experiment. Vajdi Hokmabad and Ghaemi [28] reported that the contact angle of the superhydrophobic surfaces reduces from 156° to 151° and the roll-off angle increases from 3.6° to 4.3° after 2 hours exposure to the two-phase flow. The degradation of the SHC is associated with the collision of the particles with the surface. The surface degradation is expected to be smaller in the current investigation due to smaller relaxation time (smaller number of wall collisions), smaller particle concentration (~15 particles per mm^3), and shorter exposure to the particle-laded flow (~30 min).

2.4 Particle image velocimetry

Planar PIV was applied to characterize the turbulent flow field across the channel height. Polyamide particles (VESTOSINT 2070) with an average diameter of 5 μm and density of 1.016 g/cm^3 were added as tracer particles. Illumination was provided by an Nd:YAG laser (PIV400, Spectra-Physics Inc.) with 532 nm wave length, maximum output of 400 mJ per pulse, and a maximum repetition rate of 10 Hz. A collimated laser sheet of approximately 1 mm thickness was formed using a combination of spherical and cylindrical lenses. The laser sheet was directed in the streamwise direction (*xy* plane) using a mirror sealed in an acrylic column inside the water channel as shown in Fig. 1. The lower and upper edges of the collimated laser sheet are parallel to the walls to reduce the glare line in the PIV images. The laser sheet covers a spanwise thickness of ~1 mm starting from the riblet tip for all the surfaces as shown in Fig. 2. The previous investigations by Suzuki & Kasagi [10] and Lee & Lee [12] have shown that the spanwise variation of velocity and turbulent statistics over the riblets extends up to about y^+= 10. Therefore, only the first vector in the immediate vicinity of the wall is affected by the spanwise location of the laser sheet while all the vectors farther from the wall are expected to be independent of the spanwise location of the laser with respect to the riblet tip. The laser covers slightly more than a full riblet over the s^+ = 8.6 (s = 0.75 mm) riblet while it covers a portion of the valley for larger riblets of s^+ = 17.3 and s^+ = 34.6. The first vector in the immediate vicinity of the wall provides an average value of turbulent statistics as it covered both the riblet tip and the valley.

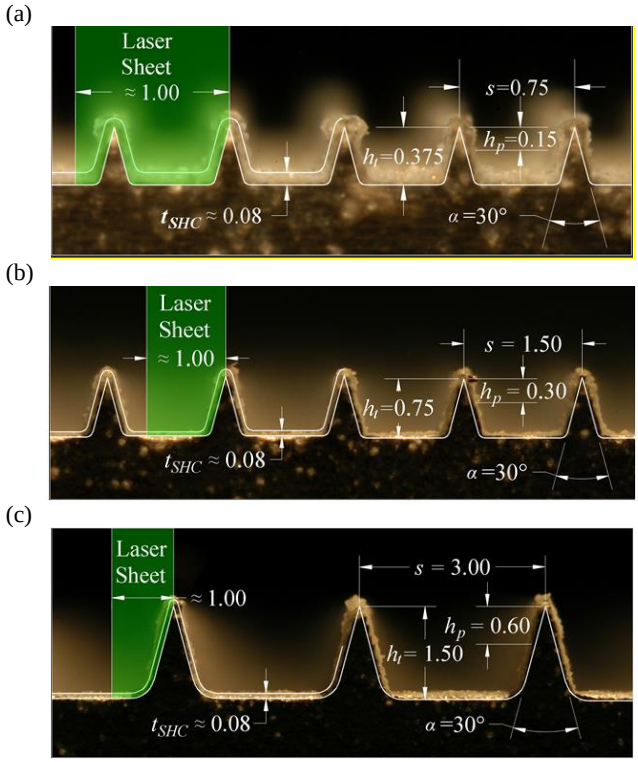

Fig. 2 Images of the cross-section of the riblets with (**a**) s^+ = 8.6, (**b**) s^+ = 17.3, (**c**) s^+ = 34.6 spacing and coated with a superhydrophobic layer of micro-size particles. All dimensions are in mm.

A 12-bit CCD camera (Imager Intense, LaVision GmbH) with sensor size of 1376×1040 pixel and a pixel size of 6.45×6.45 μm^2 collected the scattered light of the tracer particles. The camera was equipped with a 105 mm Nikkor

SLR lens at aperture size of f / 8 and imaging magnification of M = 0.2. The digital resolution and depth-of-field (DOF) were 30 pix/mm and 4.9 mm, respectively. The field-of-view (FOV) was 45.6 mm×28.6 mm (on cropped sensor size of 1376×864 pixel) extended to 5 mm upstream of the trailing-edge of the test surfaces (94H from the channel entrance and 15H from the leading-edge of test surface) as illustrated in Fig. 1. The camera frames and laser pulses were synchronized by a programmable timing unit (LaVision GmbH). An ensemble of 8,000 images over each test surface (both non-coated and coated) was recorded with a pulse separation of Δt = 3,300 μs to allow maximum displacement of 20 pix (0.67 mm) in the center of the channel in the streamwise direction.

The signal-to-noise ratio of the images was improved by subtracting the minimum intensity of the ensemble from the individual images. The images were also normalized with the ensemble average. A cross-correlation algorithm was performed over the double-frame images with final window size of 48×48 pixels (1.6 mm×1.6 mm, 0.064H×0.064H, 18.0λ×18.0λ) with 75% overlap. The vector fields were post-processed by limiting the velocity vectors from 0 to 26 pixels in the streamwise and -4 to 4 pixels in the wall-normal direction, respectively. The universal outlier detection was also applied to remove any outlier vector [32]. The double-frame images were also processed with the ensemble of correlation (EC) method [33]. The final window size in the EC method is 8×8 pixels (0.27 mm×0.27 mm, 0.011H×0.011H, 3.0λ×3.0λ) with 75% overlap. The interrogation windows are elongated in the streamwise direction with a ratio of 4:1 relative to the wall-normal dimension. All image and PIV processing was conducted using a commercial software (DaVis 8.2, LaVision GmbH). The parameters of the PIV system are summarized in Table 2.

The random error of a standard PIV system is about 0.1 pix in both streamwise and wall-normal directions according to Westerweel [34]. In the current experiment, this uncertainty is equivalent to 0.001 m/s (0.086u_τ) for measurement of mean velocity while it is 1e-6 m^2/s^2 (0.007u_τ^2) for square of velocity fluctuation. Further analysis of the random noise of the PIV is carried out using statistical convergence of the data as detailed in the Appendix section. The results show that at the peak location of Reynolds stresses, the remaining random noise is about 0.17, 0.20, and 0.25% for the $\langle u^2 \rangle$, $\langle v^2 \rangle$, and $\langle uv \rangle$ values, respectively. The estimated random noise is equivalent to 0.01u_τ^2, 0.001u_τ^2, and 0.002u_τ^2 for $\langle u^2 \rangle$, $\langle v^2 \rangle$, and $\langle uv \rangle$, respectively. The PIV bias error in the near-wall due to the glare of the laser sheet is negligible since the edge of collimated laser sheet is carefully aligned with the wall. The bias error due to the finite-size of the interrogation window is further evaluated in this work by comparing the Reynolds stresses with DNS of smooth channel flow at Re_τ = 150 [35] and also comparison of the DR of non-coated riblets with the literature.

Table 2 System parameters of the planar PIV system

Number of images	8,000	
Magnification	0.2	
Digital resolution	30 pix mm^{-1}	
Laser pulse delay	3300 μs	
Measurement domain	1376×864 pix 45.8×28.8 mm^2 529λ × 332λ	
Velocity vector	Individual correlation	Ensemble of correlation
Interrogation window (IW)	48×48 pix 1.6×1.6 mm^2 18.5λ × 18.5λ	8×8 pix 0.27×0.27 mm^2 3.1λ × 3.1λ
IW overlap	75%	
Vectors per field	104×63	672×417

3 Results and discussion

The test surfaces are placed flush mounted in the insert module of the top wall of the channel (y / H = 0) while the bottom wall at y / H = 1.0 is kept flat in all the experiments. The results are normalized using outer scaling (the average

velocity across the channel U_b and channel height H) or inner scaling (friction velocity $u_{\tau 0}$ and wall unit λ of the smooth surface). Reynolds stresses from DNS of smooth channel flow at Re_τ = 150 [35] are also provided in this section for comparison and uncertainty evaluation of the PIV measurement.

3.1 Mean velocity profile

The normalized profiles of mean velocity $<U>$ from two independent measurements over the smooth surface across the whole channel are shown in Fig. 3 (a). The overlap of the two velocity profiles confirms the repeatability of the measurement. The velocity field has a high spatial-resolution as it has been obtained using the EC method. The comparison of the $<U>$ profile with the flipped counterpart confirms its symmetry. The semi-logarithmic plot of mean velocity normalized using the inner scaling ($u^+=<U>/u_{\tau 0}$) versus wall-normal distance ($y^+ = y/\lambda_0$) is shown in Fig. 3 (b). The u^+ profiles follows the law of the wall in linear viscous sublayers ($y^+=u^+$) and the logarithmic law (k = 0.39 and B = 5.5) indicating a fully developed turbulent flow. The inner scaling is calculated here using the Clauser method [25] as reported in section II.A. Also the DNS data of Tsukahara *et al*. [35] is added to Fig. 3 (b) for comparison. The small discrepancy between the current results and the DNS is associated with smaller Re_τ = 144 of present work relative to the DNS (Re_τ = 150).

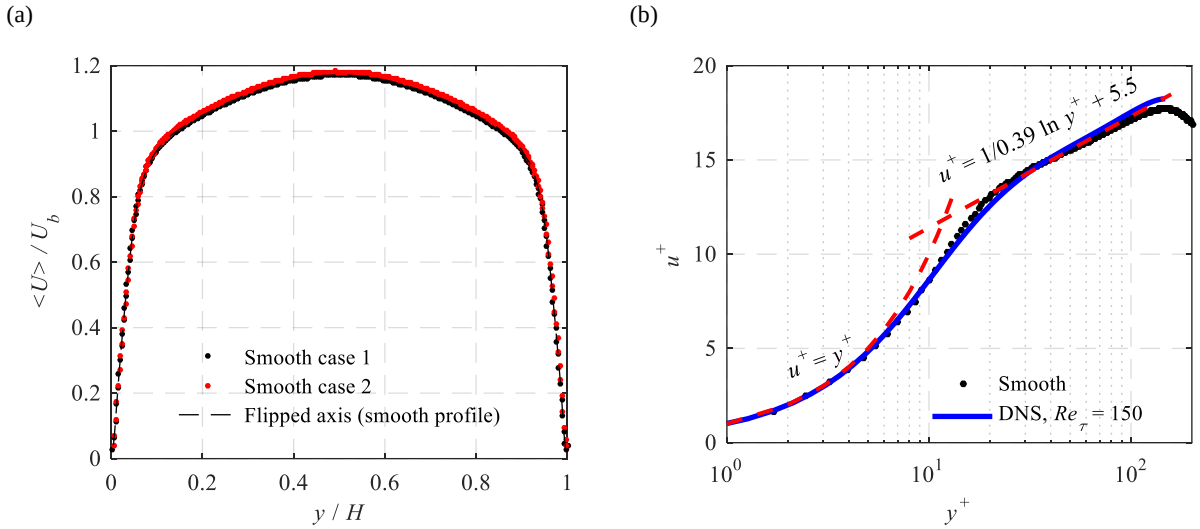

Fig. 3 (a) Mean velocity profile normalized with U_b over two smooth surface cases. (b) Semi-logarithmic plot of mean velocity over the smooth wall. The data is normalized by inner scaling obtained by Clauser method [25]. The dashed red lines show the law of the wall and the logarithmic law. The DNS data of Tsukahara *et al*. [35] is provided for comparison.

The mean velocity profile versus wall-normal distance measured from the tip of the riblet y_t up to of y_t / H = 0.2 (y_t^+ = 57) is shown in Fig. 4 (a). The lower horizontal axis shows wall normal distance normalized using the channel height while the upper horizontal axis shows y_t normalized with inner scaling of the smooth surface. The velocity over the smooth surface approaches zero at the wall as it is expected to fulfill the no-slip boundary condition. Away from $y^+ > 30$, the velocities over the smooth surface and flat with SHC overlap. The overlap of the velocity profiles over SHS in the outer layer is in agreement with the PIV measurement by Woolford et al. [36] and Vajdi Hokmabad and Ghaemi [23]. All the three riblet surfaces have larger near-wall velocity at $y_t^+ < 15$ as $<U> = 0$ (virtual origin) is located below the riblet tip ($y_t^+ < 0$). The larger is the riblet spacing, the larger is the near wall ($y_t^+ < 15$) velocity and the virtual origin is further away. In the $15 < y_t^+ < 45$ range, velocity over the large s^+ = 34.6 riblet is slightly smaller than that of the other surfaces. The difference becomes smaller with increase of wall normal distance and disappears beyond $y_t^+ > 45$ in Fig. 4(a). The reduction in slope does not indicate drag reduction as $d<U>/dy$ may change inside the riblet valley, in particular for the large s^+ = 34.6 riblets.

The mean velocity profile over the flat surface with SHC shows a slip velocity of U_s/U_b= 0.04 equivalent to U_s~0.007 m/s at the wall as shown in the inset in Fig. 4 (b). This estimation has an uncertainty of ± 0.001 m/s and is obtained by linear fit over the first six data points at $y^+ < 5$. The initial approximation of the protrusion height (h_p) shown in Fig. 2 is estimated based on the conformal mapping method of Bechert and Bartenwerfer [29]. However, this approximation does not relate h_p to variation of riblet spacing or Re. Therefore, after obtaining the velocity profiles, an extrapolation of the linear section ($y_t / H < 0.03$) to $<U> = 0$ is applied to estimate the virtual origin (y = 0) with better accuracy following Hooshmand et al. [37]. The new virtual origins for s^+ = 8.6, 17.3, and 34.6 non-coated riblets

are at y_t = -1.2λ (-0.10 mm), -3.6λ (-0.30 mm), and -8.9λ (-0.77 mm), respectively. The mean velocity profiles with respect to the estimated virtual origins ($y^+ = 0$) are shown in Fig. 4 (b). The mean velocity profile over the riblets and the counterparts with SHC are shown in Fig. 5 (a) and (b) versus the tip location of the riblets and versus the virtual origin, respectively. The velocity at the tip of the riblet (U_t) is larger over the $s^+ = 34.6$ riblet with SHC relative to U_t over the non-coated $s^+ = 34.6$ riblet. The superhydrophobic coating has resulted in a slight reduction of U_t over the $s^+ = 8.6$ and 17.3 riblets. The reduction is associated with the effect of coating roughness over the smaller riblets. The same virtual origins that were obtained from the non-coated riblets are used for the coated riblets for consistent comparison. The $s^+ = 8.6$ and $s^+ = 17.3$ riblets with SHC have slightly smaller $<U>$ at $y^+ < 15$ relative to the non-coated counterpart. This reduction of velocity is associated with the modified flow field due to the addition of the SHC. Velocity over the $s^+ = 34.6$ riblet with SHC is slightly larger than the non-coated $s^+ = 34.6$ riblet. The latter trend is similar to the slight increase of velocity in the inner layer observed over the flat surface with SHC. The observed trend suggests that the SHC may contribute to DR over the $s^+ = 34.6$ riblet. Although it is not possible to determine if the change in performance is related to a slip value or modification of the flow field inside the riblet valley since the velocity field inside the valley is not available.

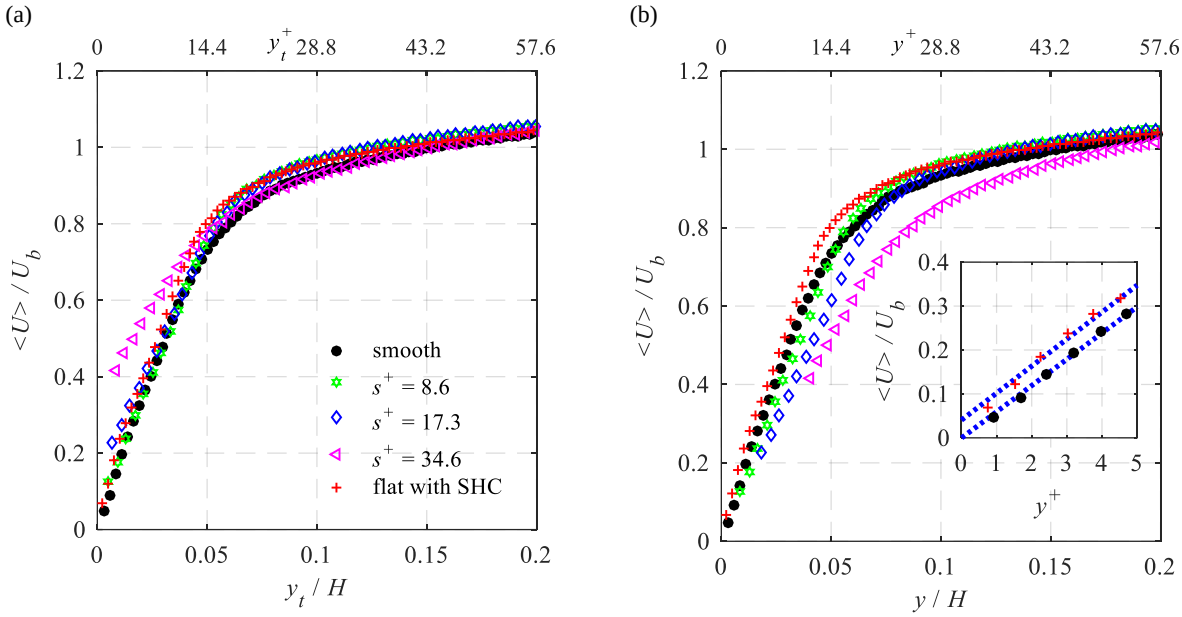

Fig. 4 (a) The near wall velocity profile obtained using ensemble of correlation method with 8 × 8 window size and 75% overlap. The wall normal distance y_t is with respect to the riblet tip. (b) The near wall velocity profiles plotted versus wall-normal distance with respect to the estimated virtual origins. The inset shows the near wall velocity profiles over smooth and flat with SHC in linear scales ($y^+ < 5$) dotted lines illustrate the linear fits.

3.2 Normal and shear Reynolds stress

The normal and shear Reynolds stresses over the smooth surface, the riblets, and the flat surface with SHC are shown in Fig. 6. The $<u^2>$ profile over all surfaces overlap across the bottom channel ($y / H > 0.5$) as seen in Fig. 6 (a). The results show smaller values of $<u^2>$ compare with the DNS data between $0.5<y/H<0.95$ associated with spatial filtering due to finite size of PIV interrogations windows. The $<u^2>$ peak is not captured due to lack of spatial resolution as the profiles monotonically increase with reduction of wall-normal distance from either wall. Fig. 6 (b) shows the normalized $<u^2>$ profiles across the upper half of the channel versus wall-normal distance in inner scaling. The profiles over the opposing bottom surface are also flipped with respect to channel centerline and shown here as solid lines for further comparison. As expected, the bottom wall profiles overlap with the $<u^2>$ profile of the smooth top wall.

Smaller value of $<u^2>$ is observed in the near wall region of $y^+ < 60$ over the riblet surfaces relative to the smooth surface and also relative to the flipped profiles of the bottom surface in Fig. 6(a). The attenuation is larger for the larger riblets although the magnitude of the $<u^2>$ peak is not available due to limited spatial resolution or lack of measurement inside the riblet valley. Choi, Moin, and Kim [11] observed 5% increase of $<u^2>$ near the riblet tip and 15% reduction of $<u^2>$ in the riblet valley for oversized $s^+ = 40$ riblets. Therefore, due to the thickness of the laser sheet in the current experiment, $<u^2>$ is expected to reduce over the riblet valley even in the DI situation of $s^+ = 34.6$. The $<u^2>$ profile over the flat surface with SHC approximately overlaps with the smooth surface profiles. The SHC is

expected to have a small effect on the $<u^2>$ peak over a limited wall-normal distance as for superhydrophobic surfaces with less than 10% DR according to DNS of Rastegari & Akhavan [38].

The profiles of $<v^2>$ normalized using the friction velocity of the bottom flat wall is presented in Fig. 6 (c) and (d). The profiles over the bottom flat surface of the channel ($y/H > 0.5$) overlap while the $<v^2>$ profile of the smooth surface shows an excellent symmetry about the center of channel. The latter is clearly observed in Fig. 6 (b) through comparison with the flipped profile. The peak of $<v^2>$ at the top wall is reduced by about 6.5 % and 11.8 % over the $s^+ = 8.6$ and 17.3 riblets, respectively. On the contrary, it increases by 9.4 % over the $s^+ = 34.6$ riblet. The $<v^2>$ peak over the flat surface with SHC decreases by 6.5 %. The peak of $<v^2>$ has approximately stayed at the same wall-normal distance for $s^+ = 8.6$ and flat with SHC while it moved slightly away from the wall over the high DR case $s^+ = 17.3$ and slightly closer to the virtual origin for the DI case of $s^+ = 34.6$.

The normalized profiles of $<uv>$ are shown in Fig. 6 (e) and (f). In a fully developed turbulent channel flows, total shear stress has a linear distribution across the channel while the contribution of the viscous shear stress is negligible in the outer layer ($y^+ > 30$). Therefore, wall shear stress can be estimated from the intercept of a linear fit over the mid-section of the $<uv>$ profile with the wall ($y^+ = 0$) and the wall shear stress is proportional to the slope of the Reynolds shear stress in the midsection. Fig 6 (e) demonstrates a linear $<uv>$ profile over the smooth surface indicting the fully developed state of the channel flow. The $<uv>$ slope changes over the riblet and flat with SHC due to applied asymmetry in the wall boundary condition (i.e., smooth wall at $y/H = 1$ while the test surface is at $y/H = 0$). The intercept of the extrapolation of the linear-fit over $0.2 < y / H < 0.5$ range with $y / H = 0$ shows 2.8% and 9.1% reduction of wall shear stress over the $s^+ = 8.6$ and 17.3 riblets relative to the smooth wall, respectively. The $s^+ = 34.6$ riblet shows increase of the intercept value relative to the smooth surface. However, this method may not be accurate since the relatively short length of the test surface ($17.2H$) does not allow formation of a fully developed flow and a linear $<uv>$ profile when testing the riblet surfaces. This is in particular visible at $y/H = 0.3$ of Fig. 6 (e) or $y^+ = 50$ of Fig. 6 (f) for the larger $s^+ = 34.6$ riblets where it significantly deviates from a straight line. A significant increase of $<uv>$ is observed at $0.1 < y / H < 0.3$ for the $s^+ = 34.6$ riblet which is an indication of higher near-wall shear and consequently higher skin-friction.

The peak value of Reynolds shear stress is also an indication of the skin-friction drag [39]. The $<uv>$ peak reduces by 6.8% and 15.3% and increases by 5.4% over the $s^+ = 8.6$, 17.3, and 34.6 riblet, respectively as shown in Fig. 6 (f). The flat surfaces with SHC coating shows 10.8% reduction of the $<uv>$ peak value relative to the smooth surface. The $<uv>$ peak is displaced away from the wall over the riblets and the SHS. The reduction in Reynolds stress peak over the flat surface with SHC is consistent with the DNS studies of Min and Kim [24] and Martell, Perot, and Rothstein [40] and also PIV measurements of Woolford *et al.* [36] and Vajdi Hokmabad and Ghaemi [23].

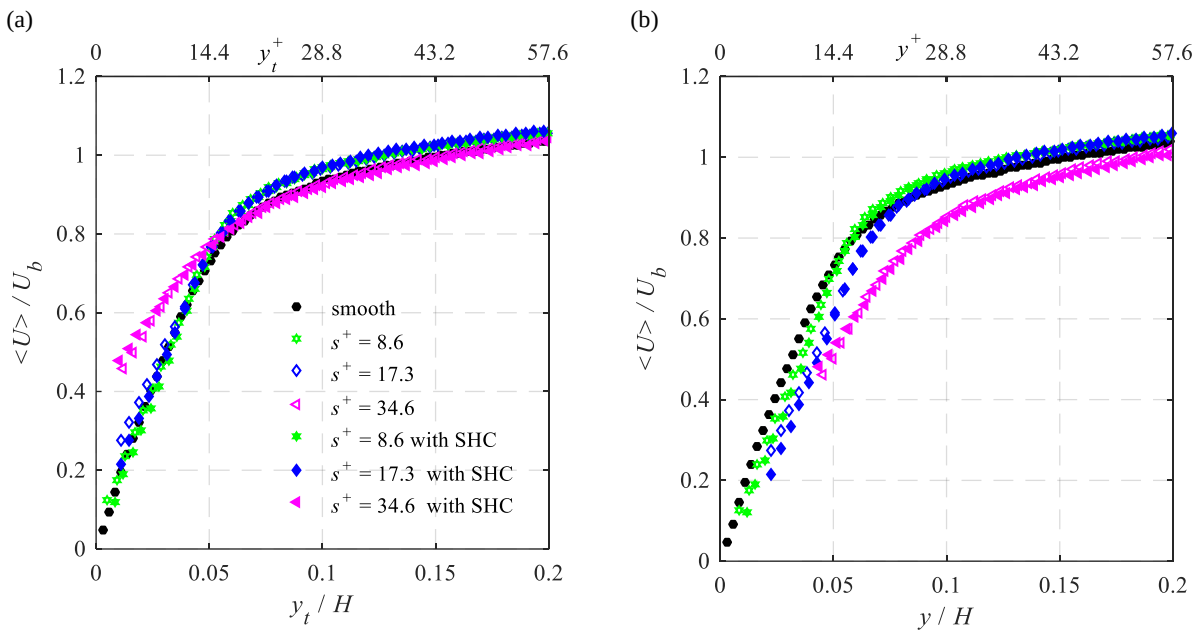

Fig. 5 Mean velocity profile over the non-coated riblets and the riblets with SHC versus wall normal distance with respect to (a) the tip location of the riblets specified by y_t, and (b) with respect to the virtual origin specified by y.

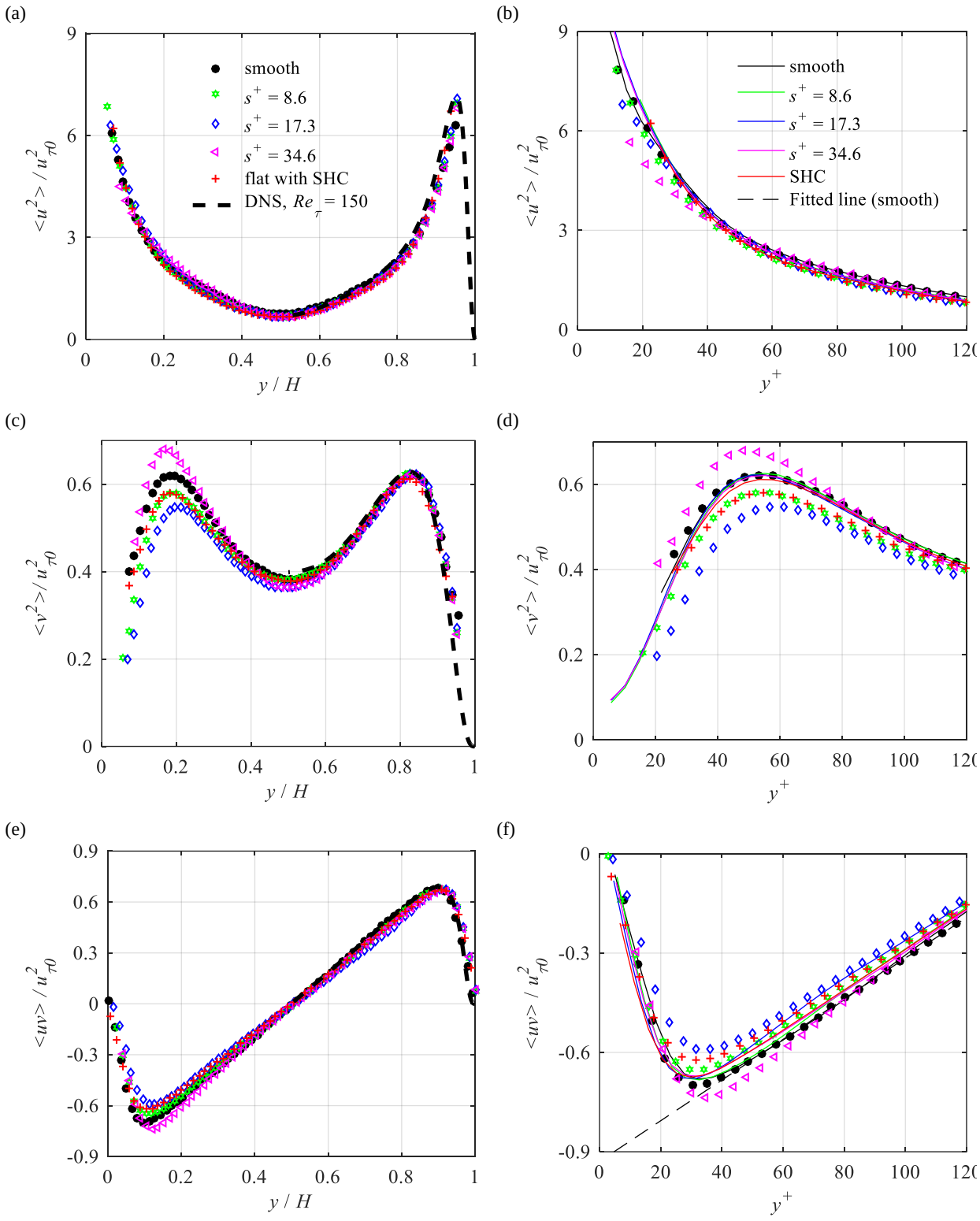

Fig. 6 Reynolds stresses over the smooth surface, the three-riblet surfaces, and the flat surface with SHC normalized using $u_{\tau 0}$ of the flat bottom surface. (a and b) Profiles of streamwise velocity fluctuation $<u^2>$, (c and d) wall-normal velocity fluctuation $<v^2>$, (e and f) and Reynolds shear stress $<uv>$ across the full channel and across the upper half of the channel, respectively. The lines in b, d, f show the profile over the bottom flat wall of the corresponding surface (flipped profile) to evaluate their overlap.

Normal and shear Reynolds stresses over the riblets and their counterparts with SHC are shown in Fig. 7. Similar to Fig 6, the lines in Fig 7 (b), (d), and (e) show the profiles over the flat bottom wall in the coordinate system of the top wall (flipped profiles) for ease of comparison. All the $<u^2>$ profiles overlap across the bottom half of the channel ($y / H > 0.5$) as seen in both Fig 7 (a) and also from the flipped profiles in Fig 7 (b). Comparison of the coated and non-coated riblet counterparts in Fig 7 (b) shows that SHC results in an increase of $<u^2>$ over the $s^+ = 8.6$ and 17.3 surfaces and a significant reduction over the $s^+ = 34.6$ riblet in the near wall region of $y^+ < 40$. The difference becomes larger with reduction of wall-normal distance.

The $<v^2>$ profile in Fig. 7 (c) and (d) overlap across the bottom half of the channel ($y / H > 0.5$). The near-wall view of Fig 7(d) shows that SHC results in negligible change of $<v^2>$ peak over the $s^+ = 8.6$ and 34.6 riblet. A large reduction of $<v^2>$ profiles is observed over s^+=17.3 riblet. The Reynolds shear stress over $s^+ = 8.6$ and s^+=17.3 riblets in Fig. 7 (e) and (f) show small difference relative to the coated counterparts. However, a large reduction of $<uv>$ is observed at the near wall region of $y^+ < 30$ after coating the s^+=34.6 riblet. A significant non-linearity is also observed in the $<uv>$ profile between $0.2 < y/H < 0.5$ for s^+=34.6 riblet with and without SHC.

The increase of $<u^2>$ after coating the $s^+ = 8.6$ and $s^+ = 17.3$ riblets with the superhydrophobic layer is associated with increase of the adverse effects of the riblet tip due to accumulation of the micro-particles as seen in Fig. 2. The superhydrophobic coating is anticipated to be ineffective in maintaining an air pocket (air plastron) at the riblet tip due to its convex geometry with small tip radius. However, the large reduction of $<u^2>$, $<v^2>$, and $<uv>$ over the s^+=34.6 riblet with SHC indicates effectiveness of the superhydrophobic coating in the riblet valley and consequently overall reduction of turbulence.

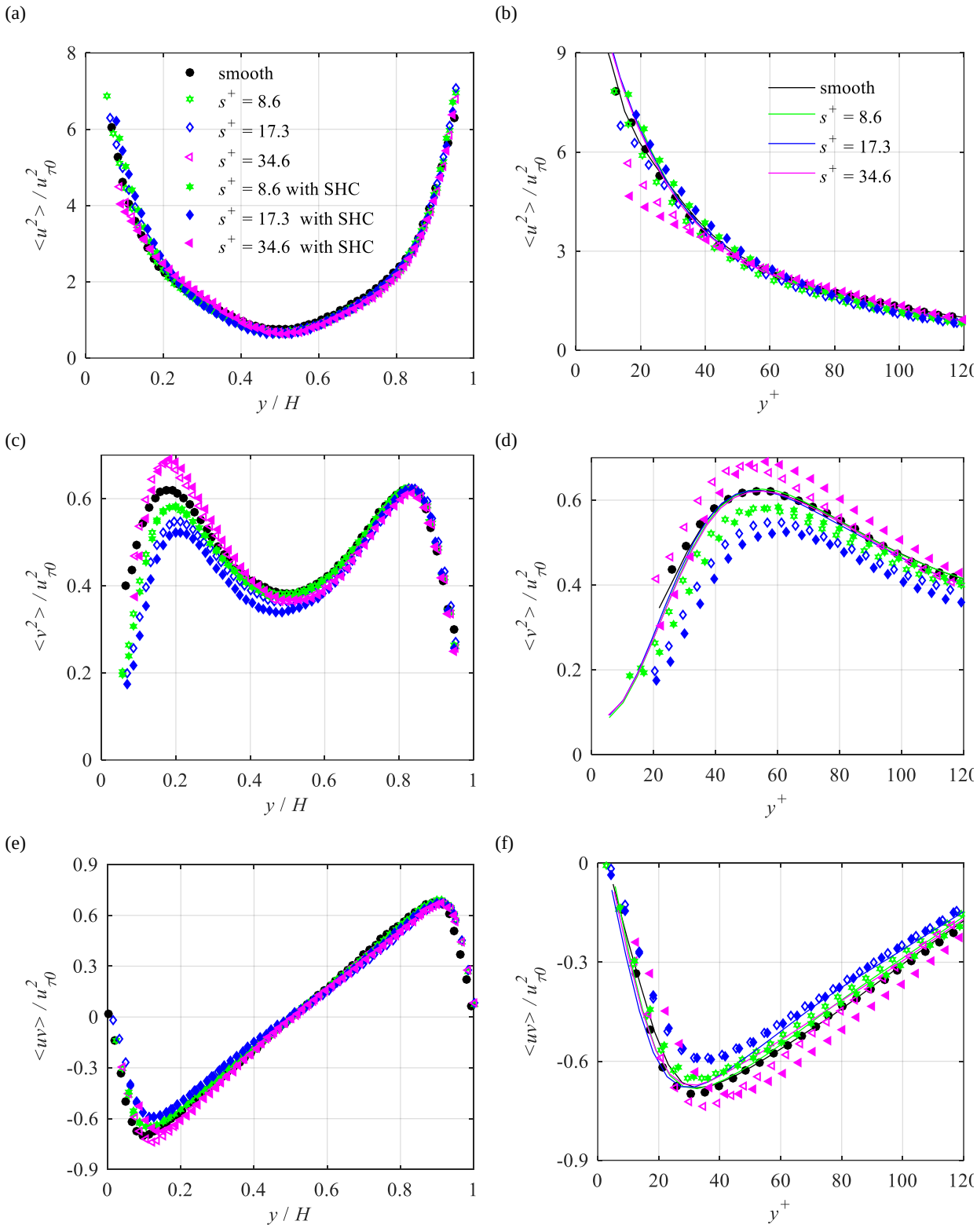

Fig. 7 Reynolds stresses over the bare riblets and riblets with SHC normalized using $u_{\tau 0}$ of the flat bottom surface. (a and b) profiles of streamwise velocity fluctuation $<u^2>$, (c and d) wall-normal velocity fluctuation $<v^2>$, (e and f) Reynolds shear stress $<uv>$ across the full channel and across the upper half of the channel, respectively. The lines in b, d, and f show the profile over the bottom flat wall (flipped profiles) of the corresponding surface to demonstrate their overlap.

3.3 Quadrant analysis

In order to investigate the effect of SHC on the turbulent fluctuations and their contribution to Reynolds shear stress, quadrant analysis is carried out close to the $<uv>$ peak where a large change in $<uv>$ was observed upon applying the SHC in Fig 7(f). The joint probability density function (JPDF) of the u and v fluctuations is plotted over the baseline smooth surface and the flat surface with SHC in Fig 8 (a). The difference of the JPDF plots as ΔJPDF = [JPDF of smooth] – [JPDF of flat with SHC] is shown in Figure 8(b) to further clarify the variation. The area covered by the 0.2% JPDF contour in the second quadrant highlighting ejection motions ($u < 0$ and $v > 0$) in Fig 8(a) becomes smaller upon applying the SHC. A similar reduction of JPDF area is also observed after applying the SHC in the fourth quadrant, which is associated with sweep motions ($u > 0$ and $v < 0$). The reduction of the enclosed area in these two quadrants indicates smaller number of strong ejection and sweep motions. This is also confirmed in Fig 8(b) since the area of strong ejections ($u/u_{\tau 0}$~ -4 and $v/u_{\tau 0}$~ 0.5) and strong sweeps ($u/u_{\tau 0}$~ 3 and $v/u_{\tau 0}$~ -1) shows a positive ΔJPDF % (red area). The blue area in Fig 8(b) shows a larger number of weak fluctuations over the flat surface with SHC. In general, Fig 8(b) shows that the strong fluctuations are attenuated (red area) while there is a larger number of weak fluctuations (core area in blue) upon applying the SHC.

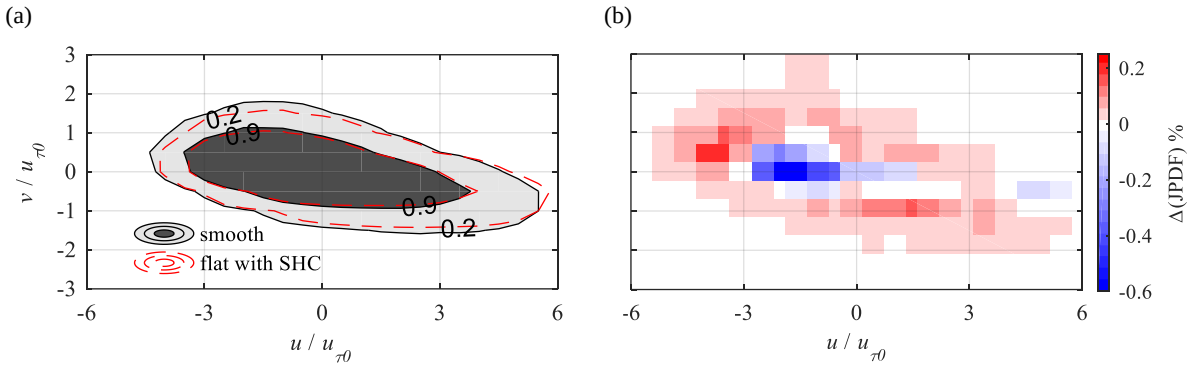

Fig. 8 (a) Joint probability density function (JPDF) showing quadrant distribution of u and v fluctuations at $y^+ = 30$ over the smooth surface (filled contours) and the flat surface with superhydrophobic coatings (dashed lines). The JPDF values are indicated as 0.2% and 0.9% for the larger and small contours, respectively. (b) The difference of the two JPDF at $y^+ = 30$ is shown as ΔJPDF = [JPDF of smooth] – [JPDF of flat with SHC] to clarify the variation.

The effect of SHC on turbulent fluctuations at $y^+ = 20$ over the three riblets is shown in Fig 9. The area enclosed by 0.2% and 0.9% JPDF contours in Fig 9 (a) for $s^+ = 8.6$ riblet with SHC has extended in the positive and negative v direction. This is more clearly seen in Fig 9 (b) as the negative ΔJPDF (blue areas) shows a larger number of strong positive and negative u fluctuations over the $s^+ = 8.6$ riblet with SHC. The ΔJPDF contours of Fig 9(b) also show that the wall normal fluctuations attenuate over the surface with SHC. Therefore, a larger number of strong sweep and ejection motions is present over the undersized riblet with SHC. These observations are consistent with the increase of $<u^2>$ and small reduction of $<v^2>$ observed in Fig 7 after coating the $s^+ = 8.6$ riblet. SHC has a similar effect, although weaker, on turbulent fluctuations on the $s^+ = 17.3$ riblet as shown in Fig. 9 (c) and (d). However, an opposite trend is observed upon SHC of the large $s^+ = 34.6$ riblet as shown in Fig 9 (e) and (f). The area of JPDFs in Figure 9(e) becomes smaller in the second and fourth quadrants by applying the SHC. The ΔJPDF of Fig 9(f) shows a smaller number of strong ejection and sweep motions over the coated surface indicated by the positive ΔJPDF (red areas) at [$u/u_{\tau 0}$~ -4 and $v/u_{\tau 0}$~ +0.5] and [$u/u_{\tau 0}$~ +4 and $v/u_{\tau 0}$~ -0.5], respectively. There is an area with negative ΔJPDF (blue) at the center of the quadrant, which indicates a larger number of weak fluctuations over $s^+ = 34.6$ riblet with SHC.

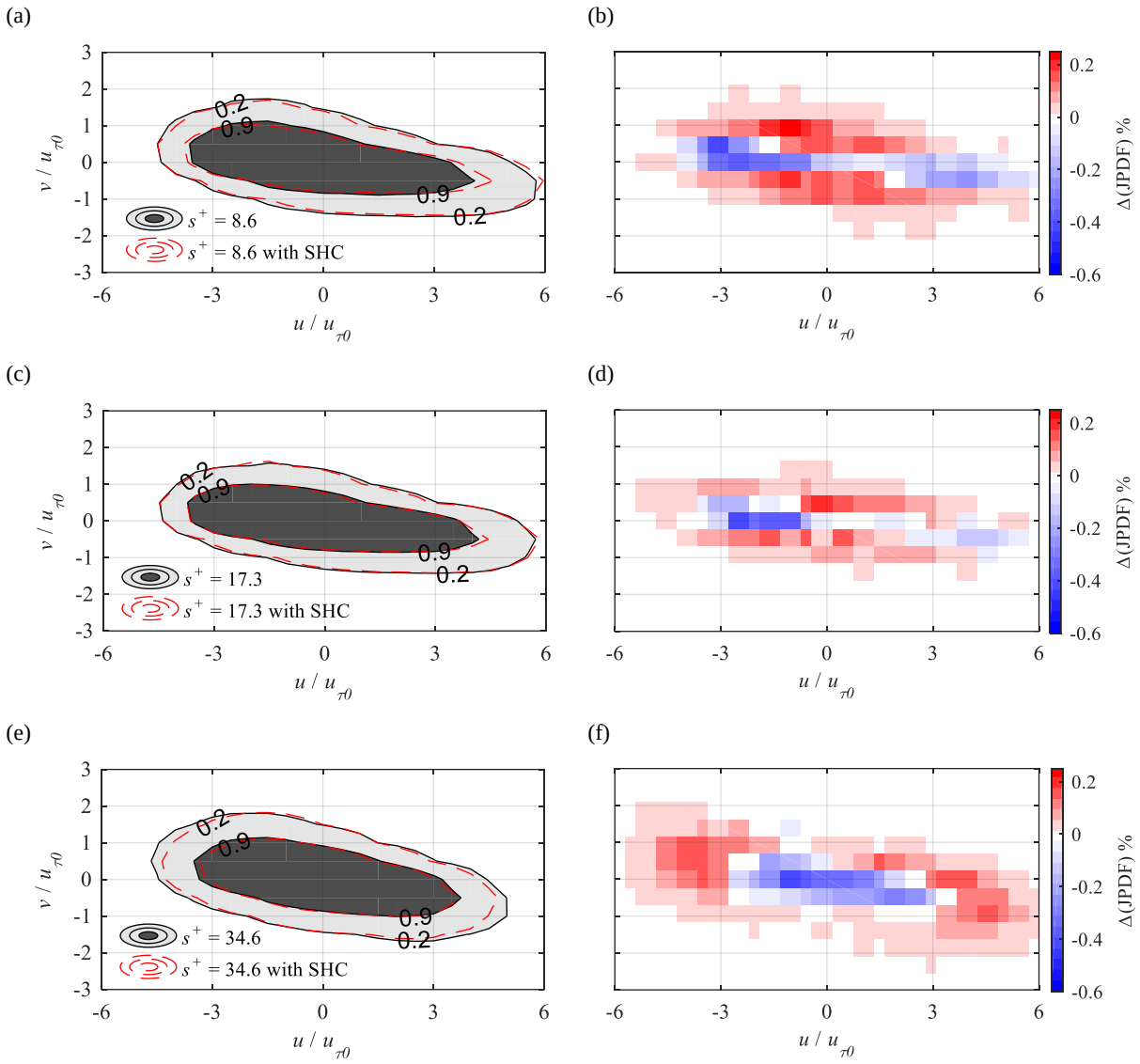

Fig. 9 JPDF of streamwise and wall-normal fluctuations at $y^+ = 20$ over (a) $s^+ = 8.6$, (c) $s^+ = 17.3$, and (e) $s^+ = 34.6$ riblet with SHC (dashed contours) and without SHC (filled contours). The dark gray and light gray colors in the filled contours along with the red line contours near each level of gray denote pdf values 0.2% and 0.9%, respectively. The difference of the two JPDF at $y^+ = 30$ is shown as ΔJPDF = [JPDF of smooth] – [JPDF of flat with SHC] for (b) $s^+ = 8.6$, (d) $s^+ = 17.3$, and (f) $s^+ = 34.6$ riblets to clarify the variations.

3.4 Wall shear stress

Measurement of small changes in skin-friction drag over short superhydrophobic samples using direct force measurement or pressure drop measurement is challenging, due to the small bulk velocity in the channel. The small bulk velocity was chosen to obtain a large wall-unit (larger turbulent structures) for spatially resolved PIV of turbulent statistics. In addition, the $\langle uv \rangle$ profile of the larger riblet did not follow a straight line in the mid-section of the channel, which prevents estimation of wall-shear stress based on the $\langle uv \rangle$ slope. This is because the flow doesn't achieve a fully developed state over relatively short length of the superhydrophobic/riblet surface. Therefore, the skin friction coefficient C_f is obtained by integrating the streamwise Reynolds-averaged momentum equation for a turbulent channel flow from the tip of the riblet ($h_t / h = 0$) to the middle of the channel ($y / h = 1$). The same approach as Fukagata *et al.* [41] is followed, while the boundary conditions for $\langle U \rangle$ and $\langle uv \rangle$ at the riblet tip is set to U_t and $\langle uv \rangle_t$, respectively. The expression for C_f is obtained as

$$C_f = \frac{6}{Re_b}\left(1 - \frac{U_t}{U_b}\right) + 2\left(\frac{-\langle uv\rangle_t}{U_b^2}\right) + 6\int_{h_t/h}^{1}(1-\delta)\left(\frac{-\langle uv\rangle}{U_b^2}\right)d\delta. \quad (1)$$

Here Re_b is Reynolds number based on the bulk velocity and half channel height (h), δ is the normalized wall normal coordinate (y / h). The skin-friction coefficient (C_f^0) over the smooth surface is obtained from Fukagata *et al.* [41] with integration limits from 0 to the mid-channel height (y/h = 1)

$$C_f^0 = \frac{6}{Re_b} + 6\int_0^1(1-\delta)\left(\frac{-\langle uv\rangle}{U_b^2}\right)d\delta. \quad (2)$$

The estimations of C_f and C_f^0 over the riblets and smooth surface using Equation 1 and 2, respectively, is applied to obtain the DR percentages using

$$\mathrm{DR} = \frac{C_f^0 - C_f}{C_f^0} \quad (3)$$

The DR estimations are shown in Table 3. As it is expected, the non-coated s^+=8.6 and 17.3 riblet result in 4.8% and 7.5% reduction in drag while the over-sized s^+ = 34.6 riblet increases drag by 9.0%. These values are close to the estimations based on Bechert *et al*. [6] presented in Table 1. Improvement of the DR percentages is observed in Table 3 over all riblets when coated with the SHC. The DR percentages increases over s^+ = 8.6 and 17.3 riblets with SHC by 1.2 and 2.6%, respectively. However, a large improvement (10.2%) is obtained over the s^+ = 34.6 riblet, which transferred this over-sized riblet from DI to DR regime. It is speculated that the observed improvement is as a result of the effectiveness of the SHC in the larger valleys of the over-sized riblet. The C_f over the flat surface with SHC is also calculated using Equation 1 with integration limits from h_t = 0 to the mid-channel height with boundary conditions of U_s = 0.007 m/s instead of U_t, and $\langle uv\rangle_t$ =0 at the wall. This results in 6.9% reduction of skin-friction on the flat surface.

Table 3 Estimation of the DR percentage based on comparison with the smooth wall.

Surface	**DR%**
s^+ = 8.6	4.8
s^+ = 17.3	7.5
s^+ = 34.6	-9.0
s^+ = 8.6 with SHC	6.0
s^+ = 17.3 with SHC	10.1
s^+ = 34.6 with SHC	1.2
Flat surface with SHC	6.9

Fig 10 shows the DR diagram for different sizes of trapezoidal riblets with $\alpha = 30^\circ$ based on experiments of Bechert *et al*. [6]. There is a good overlap of previous data for $s^+ < 24$, showing the maximum DR at about s^+=17. The shaded area shows the DR percentages estimated for $s^+ > 24$ riblets by extrapolating Bechert *et al*. [6] data due to sparse data points. The DR values of the current experiment over the three tested riblets show an acceptable overlap with Bechert *et al*. [6] results although there is an underestimation of DR for the small s^+ = 8.6 riblet. The SHC increases DR percentages over all the tested riblets while DR improvement increases with the increase of the riblets spacing.

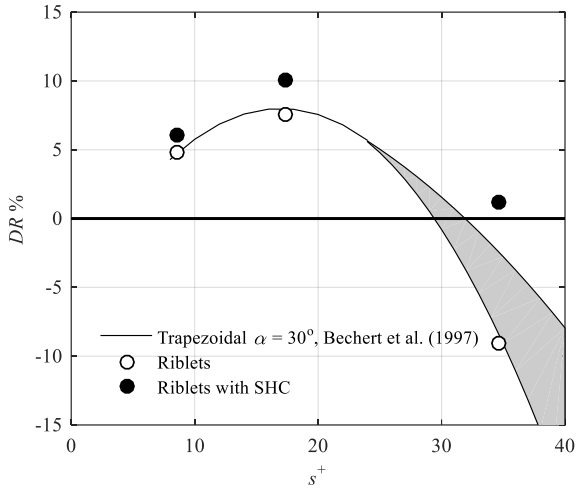

Fig. 10 The DR percentage over the trapezoidal riblets and riblets with SHC. The shaded area shows the range of extrapolation based on Bechert *et al*. [6] data (beyond $s^+ > 24$).

4 Drag reduction mechanism

Drag reduction over riblets with SHC depends on the tip spacing of the riblets. The percentage and the mechanism of DR over the undersized riblets ($s^+<10$) or riblets with optimum spacing ($s^+\sim15$) are not affected by the superhydrophobic coating. For drag-reducing riblets ($s^+ < 25$), the streamwise vortices are away from the valley of riblets, causing reduction of skin-friction drag. When the riblet is coated with the superhydrophobic material, the air layer in the valley of the coated riblets is not in contact with the vortcies, and does not affect the DR illustrated in Fig 11. However, for oversized riblets ($s^+ > 25$), some of the turbulence structures enter the valley of the riblet, and become in contact with the valley surface. In this case, the addition of the superhydrophobic coating and the air layer, changes the drag reduction mechanism to attenuation of wall turbulence due to slip velocity. It is conjectured that the shape of the riblet valley forms a thicker air layer and larger slip velocity. The air layer is also protected by the smaller velocity and lower turbulence in the valley of the riblet.

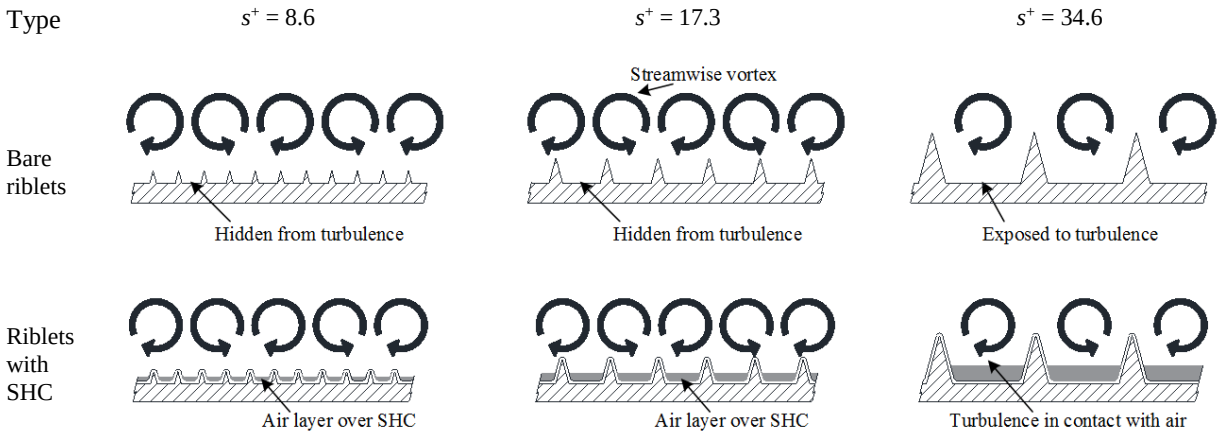

Fig. 11. A schematic view of drag reduction mechanism using the combination of SHC and riblet surfaces with different tip spacing. The air layer is only effective for DR in the valley of the oversized (s^+=34.6) riblet, since the streamwise vortices can enter the valley and are in contact with the air layer. The air layer in the valley of the smaller s^+=8.6 and 17.3 riblet does not help with DR as it is not in contact with the streamwise vortices of the near wall turbulence.

5 Conclusion

The turbulent flow over riblet surfaces with superhydrophobic coating and their DR performance was investigated by means of a planar PIV in a turbulent channel flow at Re_τ = 144. The evaluation was carried out on undersized (low DR), optimum (maximum DR), and oversized (drag increase) riblet surfaces with non-dimensional tip spacing of s^+ = 8.6, 17.3 and 34.6, respectively. The three bare riblet surfaces, counterpart surfaces coated with a superhydrophobic layer and flat surfaces with and without superhydrophobic coating were investigated.

The results show smaller mean velocity $y^+ < 15$ over the s^+ = 8.6 and s^+ = 17.3 riblets after applying the SHC relative to the non-coated counterparts. Investigation of turbulence statistics showed small increase of $<u^2>$ over the s^+ = 8.6 and s^+ = 17.3 riblets while reduction of $<v^2>$ was observed in the near-wall region. The Reynolds shear stress over s^+ = 8.6 and s^+ = 17.3 riblets did not show a considerable variation relative to the coated counterparts. The estimation of drag reduction based on weighted integral of $<uv>$ (without any slip velocity term) showed a lower limit of an additional 1.2 and 2.6% DR after coating the s^+ = 8.6 and s^+ = 17.3 riblets, respectively.

The mean velocity in the near-wall region (y/H<0.05) of the oversized riblet with tip spacing of s^+ = 34.6 increased after applying the SHC. The Reynolds stresses including $<u^2>$, $<v^2>$, and $<uv>$ were reduced over the s^+ = 34.6 riblet at $y^+ < 50$. The DR performance of this riblet also improved from 9.0% DI to 1.2% DR after coating the surface. The improvement was associated with the attenuation of ejection and sweep motions over this riblet as observed in the quadrant analysis. The investigations showed that the SHC is more effective on larger riblet surfaces where wall-turbulence and streamwise vortices are present inside the riblet valley.

Acknowledgments

This work has been supported by the Natural Sciences and Engineering Research Council of Canada (NSERC RGPIN 1512 GHAEMI and STPGP 478987 SHANKAR).

Appendix: uncertainty analysis

The random error of the measurements is associated with a variety of sources including PIV random noise, vibration of the facility, and variation in pump performance. The random noise of the turbulence statistics is evaluated using the statistical convergence of $<u^2>/u_{\tau 0}$, $<v^2>/u_{\tau 0}$, and $<uv>/u_{\tau 0}$ for all the surfaces as shown in Fig 12, 13, and 14, respectively. The results show that the turbulence statistics reach steady-state (i.e., statistical convergence) after about 1,000 seconds for all the surfaces. The random error (ε_r) is evaluated as the standard deviation of the data between 1,000 to 1,600 seconds. The average ε_r for all the surfaces is $0.01u_\tau^2$, $0.001u_\tau^2$, and $0.002u_\tau^2$ for $<u^2>$, $<v^2>$, and $<uv>$, respectively. The statistical convergence of the mean values over the surfaces with SHC also indicates the longevity of the air layer during the measurements.

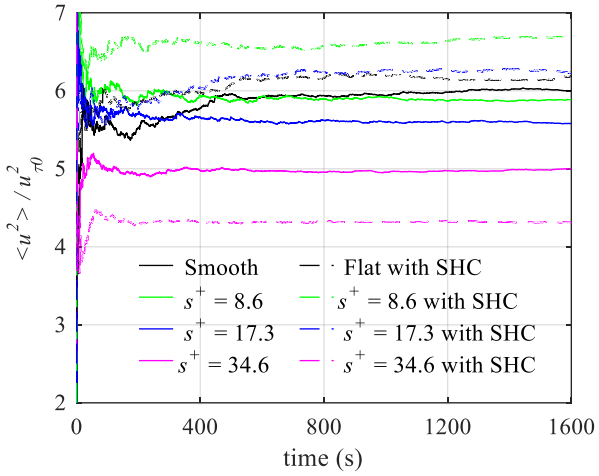

Fig. 12 Statistical convergence of $<u^2>/u_{\tau 0}$ versus time at $y^+ \approx 20$.

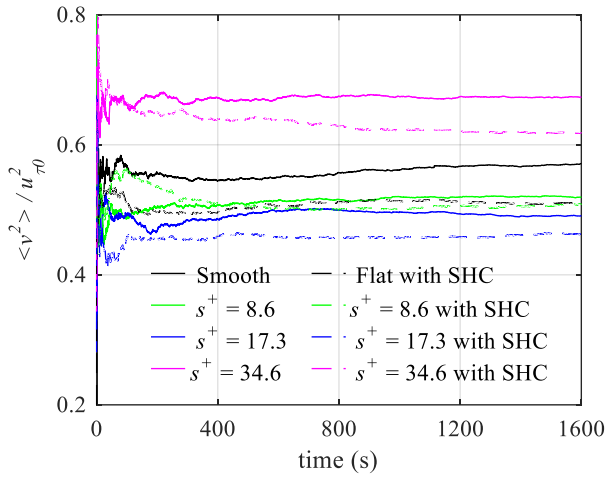

Fig. 13 Statistical convergence of $<v^2>/u_{\tau 0}$ versus time at the peak location ($y^+ \approx 40$).

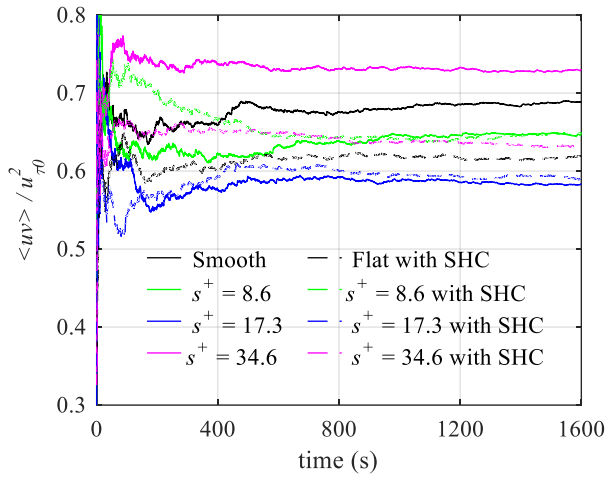

Fig. 14 Statistical convergence of $<uv>/u_{\tau 0}$ versus time at peak location ($y^+ \approx 30$).

In order to estimate the uncertainty of the JPDF in Fig 8 and 9, statistical convergence of the JPDF value is evaluated at u/u_τ = -3.25 and v/u_τ = 0.5 over a two-dimensional bin with dimension of 0.5 u_τ and 0.5 u_τ. The bin size corresponds to the grid size applied in Fig 8 and 9 for calculation of the JPDF. The results in Fig 14 show statistical convergence of all the data after about 1000 seconds. The results show that the variation in the JPDF value is smaller than the difference between the uncoated and coated counterparts in Figures (a), (b), and (d). The standard deviation of the JPDF fluctuations is about 0.01 in Figure 15.

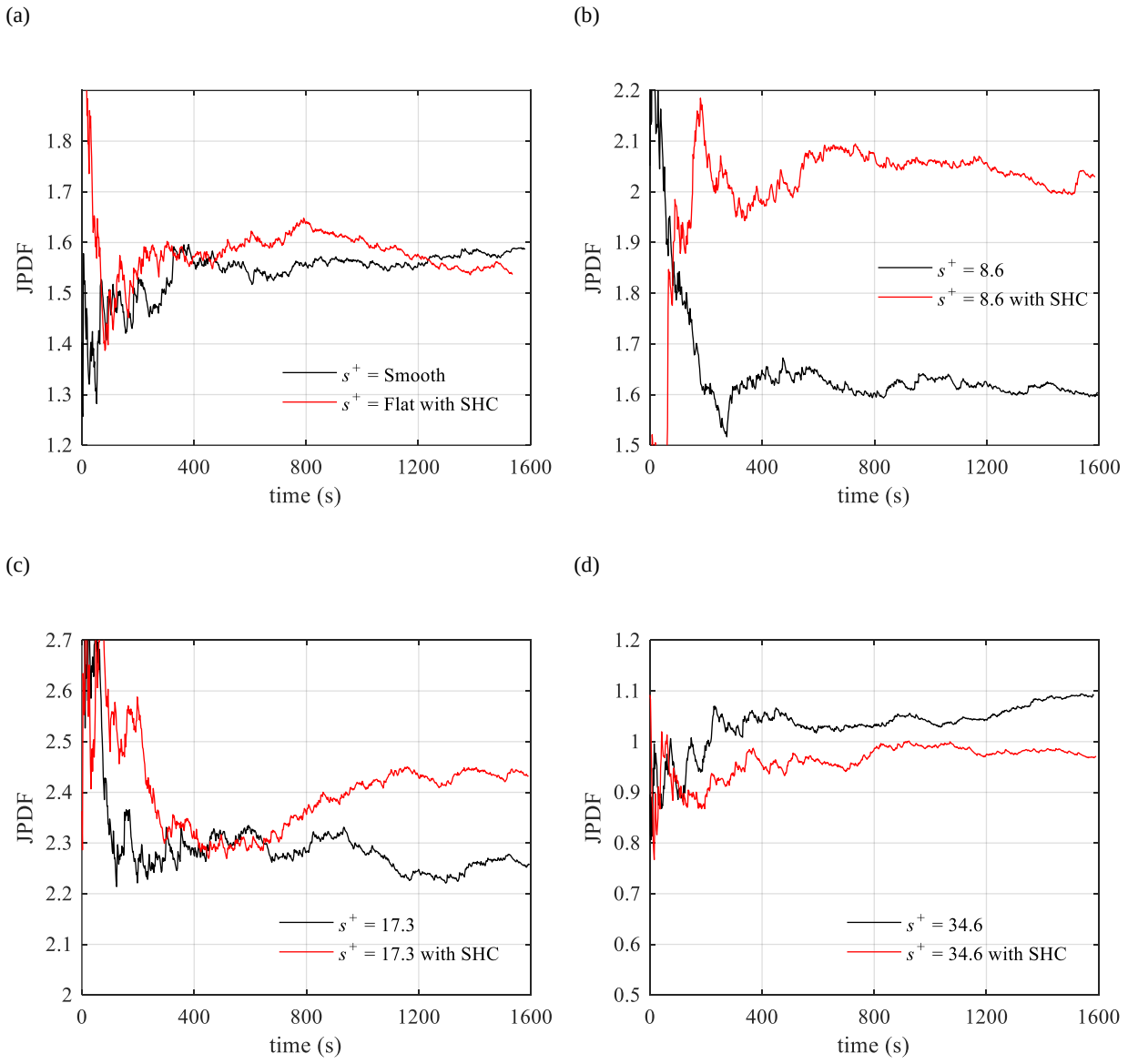

Fig. 15 Convergence of JPDF over (a) smooth and flat surface with SHC, (b) s^+ = 8.6, (c) s^+ = 17.3, and (d) s^+ = 34.6 riblet with and without SHC at u/u_τ = -3.25 and v/u_τ = 0.5.

Reference

[1] M. D. Warholic, H. Massah, and T. J. Hanratty, "Influence of drag-reducing polymers on turbulence: effects of Reynolds number, concentration and mixing," *Exp. Fluids*, vol. 27, no. 5, pp. 461–472, Oct. 1999.

[2] M. E. McCormick and R. Bhattacharyya, "Drag reduction of a submersible hull by electrolysis," *Nav. Eng. J.*, vol. 85, no. 2, pp. 11–16, Apr. 1973.

[3] R. J. Daniello, N. E. Waterhouse, and J. P. Rothstein, "Drag reduction in turbulent flows over superhydrophobic surfaces," *Phys. Fluids*, vol. 21, no. 8, p. 85103, 2009.

[4] M. J. Walsh, "Riblets as a Viscous Drag Reduction Technique," *AIAA J.*, vol. 21, no. 4, pp. 485–486, Apr. 1983.

[5] M. Walsh and A. Lindemann, "Optimization and application of riblets for turbulent drag reduction," in *22nd Aerospace Sciences Meeting*, 1984, pp. 1–10.

[6] D. W. Bechert, M. Bruse, W. Hage, J. G. T. Van Der Hoeven, and G. Hoppe, "Experiments on drag-reducing surfaces and their optimization with an adjustable geometry," *J. Fluid Mech.*, vol. 338, pp. 59–87, May 1997.

[7] M. J. Walsh, "Drag characteristics of V-groove and transverse curvature riblets," in *Symposium on Viscous flow drag reduction*, 1979, pp. 168–184.

[8] R. García-Mayoral and J. Jiménez, "Hydrodynamic stability and breakdown of the viscous regime over riblets," *J. Fluid Mech.*, vol. 678, no. 2011, pp. 317–347, Jul. 2011.

[9] S. K. Robinson, "Coherent Motions in the Turbulent Boundary Layer," *Annu. Rev. Fluid Mech.*, vol. 23, no. 1, pp. 601–639, Jan. 1991.

[10] Y. Suzuki and N. Kasagi, "Turbulent drag reduction mechanism above a riblet surface," *AIAA J.*, vol. 32, no. 9, pp. 1781–1790, Sep. 1994.

[11] H. Choi, P. Moin, and J. Kim, "Direct numerical simulation of turbulent flow over riblets," *J. Fluid Mech.*, vol. 255, no. 1, p. 503, Oct. 1993.

[12] S. J. Lee and S. H. Lee, "Flow field analysis of a turbulent boundary layer over a riblet surface," *Exp. Fluids*, vol. 30, no. 2, pp. 153–166, Feb. 2001.

[13] J. Kim, P. Moin, and R. Moser, "Turbulence statistics in fully developed channel flow at low Reynolds number," *J. Fluid Mech.*, vol. 177, pp. 133–166, 1987.

[14] R. García-Mayoral and J. Jiménez, "Scaling of turbulent structures in riblet channels up to Re $\tau \approx 550$," *Phys. Fluids*, vol. 24, no. 10, p. 105101, Oct. 2012.

[15] C. Barbier, E. Jenner, and B. D'Urso, "Drag Reduction With Superhydrophobic Riblets," in *Volume 8: Mechanics of Solids, Structures and Fluids*, 2012, p. 199.

[16] J. F. Prince, D. Maynes, and J. Crockett, "Pressure Drop Measurements in Turbulent Channel Flow Over Superhydrophobic Surfaces With Riblets," in *ASME 2014 12th International Conference on Nanochannels, Microchannels and Minichannels*, 2014, p. V001T08A004.

[17] C. Neinhuis and W. Barthlott, "Characterization and Distribution of Water-repellent, Self-cleaning Plant Surfaces," *Ann. Bot.*, vol. 79, no. 6, pp. 667–677, Jun. 1997.

[18] S. H. Kim, "Fabrication of Superhydrophobic Surfaces," *J. Adhes. Sci. Technol.*, vol. 22, no. 3–4, pp. 235–250, Jan. 2008.

[19] J. P. Rothstein, "Slip on Superhydrophobic Surfaces," *Annu. Rev. Fluid Mech.*, vol. 42, no. 1, pp. 89–109, Jan. 2010.

[20] J. Ou, B. Perot, and J. P. Rothstein, "Laminar drag reduction in microchannels using ultrahydrophobic surfaces," *Phys. Fluids*, vol. 16, no. 12, p. 4635, 2004.

[21] J. Ou and J. P. Rothstein, "Direct velocity measurements of the flow past drag-reducing ultrahydrophobic surfaces," *Phys. Fluids*, vol. 17, no. 10, p. 103606, 2005.

[22] T. O. Jelly, S. Y. Jung, and T. A. Zaki, "Turbulence and skin friction modification in channel flow with streamwise-aligned superhydrophobic surface texture," *Phys. Fluids*, vol. 26, no. 9, p. 95102, Sep. 2014.

[23] B. Vajdi Hokmabad and S. Ghaemi, "Turbulent flow over wetted and non-wetted superhydrophobic counterparts with random structure," *Phys. Fluids*, vol. 28, no. 1, p. 15112, Jan. 2016.

[24] T. Min and J. Kim, "Effects of hydrophobic surface on skin-friction drag," *Phys. Fluids*, vol. 16, no. 7, pp. 0–3, 2004.

[25] F. H. Clauser, "The Turbulent Boundary Layer," in *Advances in Applied Mechanics*, vol. 4, no. C, 1956, pp. 1–51.

[26] R. N. Govardhan, G. S. Srinivas, A. Asthana, and M. S. Bobji, "Time dependence of effective slip on textured hydrophobic surfaces," *Phys. Fluids*, vol. 21, no. 5, p. 52001, 2009.

[27] M. A. Samaha, H. V. Tafreshi, and M. Gad-el-Hak, "Superhydrophobic surfaces: From the lotus leaf to the submarine," *Comptes Rendus Mécanique*, vol. 340, no. 1–2, pp. 18–34, Jan. 2012.

[28] B. Vajdi Hokmabad and S. Ghaemi, "Effect of Flow and Particle-Plastron Collision on the Longevity of Superhydrophobicity," *Sci. Rep.*, vol. 7, p. 41448, Jan. 2017.

[29] D. W. Bechert and M. Bartenwerfer, "The viscous flow on surfaces with longitudinal ribs," *J. Fluid Mech.*, vol. 206, pp. 105–129, Sep. 1989.

[30] R. Grüneberger and W. Hage, "Drag characteristics of longitudinal and transverse riblets at low dimensionless spacings," *Exp. Fluids*, vol. 50, no. 2, pp. 363–373, Feb. 2011.

[31] R. A. Bidkar, L. Leblanc, A. J. Kulkarni, V. Bahadur, S. L. Ceccio, and M. Perlin, "Skin-friction drag reduction in the

turbulent regime using random-textured hydrophobic surfaces," *Phys. Fluids*, vol. 26, no. 8, p. 85108, Aug. 2014.

[32] J. Westerweel and F. Scarano, "Universal outlier detection for PIV data," *Exp. Fluids*, vol. 39, no. 6, pp. 1096–1100, Dec. 2005.

[33] C. D. Meinhart, S. T. Wereley, and J. G. Santiago, "A PIV Algorithm for Estimating Time-Averaged Velocity Fields," *J. Fluids Eng.*, vol. 122, no. 2, p. 285, 2000.

[34] J. Westerweel, "Fundamentals of digital particle image velocimetry," *Meas. Sci. Technol.*, vol. 8, no. 12, pp. 1379–1392, Dec. 1997.

[35] T. Tsukahara, Y. Seki, H. Kawamura, and D. Tochio, "DNS of turbulent channel flow at very low Reynolds numbers," in *International symposium on turbulence and shear flow phenomena (TSFP-4)*, 2005, pp. 935–940.

[36] B. Woolford, J. Prince, D. Maynes, and B. W. Webb, "Particle image velocimetry characterization of turbulent channel flow with rib patterned superhydrophobic walls," *Phys. Fluids*, vol. 21, no. 8, 2009.

[37] D. Hooshmand, R. Youngs, J. M. Wallace, and J. L. Balint., "An experimental study of changes in the structure of a turbulent boundary layer due to surface geometry changes," *AIAA J.*, pp. 83–0230, 1983.

[38] A. Rastegari and R. Akhavan, "On the mechanism of turbulent drag reduction with super-hydrophobic surfaces," *J. Fluid Mech.*, vol. 773, p. R4, Jun. 2015.

[39] J. S. Paschkewitz *et al.*, "An experimental and numerical investigation of drag reduction in a turbulent boundary layer using a rigid rodlike polymer," *Phys. Fluids*, vol. 17, no. 8, p. 85101, 2005.

[40] M. B. Martell, J. B. Perot, and J. P. Rothstein, "Direct numerical simulations of turbulent flows over superhydrophobic surfaces," *J. Fluid Mech.*, vol. 620, pp. 31–41, Feb. 2009.

[41] K. Fukagata, K. Iwamoto, and N. Kasagi, "Contribution of Reynolds stress distribution to the skin friction in wall-bounded flows," *Phys. Fluids*, vol. 14, no. 11, p. L73, 2002.